Weierstraß-Institut
für Angewandte Analysis und Stochastik
Leibniz-Institut im Forschungsverbund Berlin e. V.

Preprint ISSN 0946 – 8633

Self-heating effects in organic semiconductor devices enhanced by positive temperature feedback

Axel Fischer[1], Paul Pahner[1], Björn Lüssem[1], Karl Leo[1], Reinhard Scholz[1],

Thomas Koprucki [2], Jürgen Fuhrmann[2], Klaus Gärtner[2], Annegret Glitzky[2]

submitted: 9 March, 2012

[1] Institut für Angewandte Photophysik (IAPP)
Technische Universität Dresden
George-Bähr-Straße 1
01069 Dresden, Germany
E-Mail: axel.fischer@iapp.de
paul.pahner@iapp.de
bjoern.luessem@iapp.de
karl.leo@iapp.de
reinhard.scholz@iapp.de

[2] Weierstraß-Institut
Mohrenstraße 39
10117 Berlin
Germany
E-Mail: thomas.koprucki@wias-berlin.de
juergen.fuhrmann@wias-berlin.de
klaus.gaertner@wias-berlin.de
annegret.glitzky@wias-berlin.de

No. 1693
Berlin 2012

2010 *Mathematics Subject Classification.* 80A20, 35K05, 35C05, 65N08.

Key words and phrases. Heat conductivity, organic semiconductor, C_{60}, crossbar electrodes, Joule heating, device temperature, thermal resistance, break down, analytical solution, heat frow equation, 3D simulation, finite volume method.

The authors thank IPMS Fraunhofer (Dresden) for use of the infrared camera. The work of Th. Koprucki has been supported by the Deutsche Forschungsgemeinschaft (DFG) within the collaborative research center SFB 787 Semiconductor Nanophotonics. The work leading to these results has received funding from the European Communitys Seventh Framework Programme under Grant Agreement No. FP7-267995 (NUDEV).

Edited by
Weierstraß-Institut für Angewandte Analysis und Stochastik (WIAS)
Leibniz-Institut im Forschungsverbund Berlin e. V.
Mohrenstraße 39
10117 Berlin
Germany

Fax: +49 30 2044975
E-Mail: preprint@wias-berlin.de
World Wide Web: http://www.wias-berlin.de/

Abstract. We studied the influence of heating effects in an organic device containing a layer sequence of n-doped / intrinsic / n-doped C_{60} between crossbar metal electrodes. A strong positive feedback between current and temperature occurs at high current densities beyond $100\,A/cm^2$, as predicted by the extended Gaussian disorder model (EGDM) applicable to organic semiconductors. These devices give a perfect setting for studying the heat transport at high power densities because C_{60} can withstand temperatures above 200°C. Infrared images of the device and detailed numerical simulations of the heat transport demonstrate that the electrical circuit produces a superposition of a homogeneous power dissipation in the active volume and strong heat sources localized at the contact edges. Hence, close to the contact edges, the current density is significantly enhanced with respect to the central region of the device, demonstrating that three-dimensional effects have a strong impact on a device with seemingly one-dimensional transport.

1. Introduction

Over the last few years, electronic devices based on organic semiconductors have received increasing attention. Especially organic light emitting diodes (OLED) and organic solar cells (OSC) have reached a mature stage allowing for commercialization.

On the other hand, although organic field effect transistors (OFETs) are already used in first products such as e-readers or radio frequency identification (RFID) tags, the full commercialization of OFETs is severely hampered by the low charge carrier mobility of organic semiconductors which limits the switching frequency and the saturation current. One approach to overcome these limits is to reduce the channel length, which however involves the use of sophisticated structuring methods [1]. A solution to this problem is the use of vertical transistors, where the active length can be controlled down to a few nanometers by varying the thickness of the organic layers [2, 3, 4]. Independent of the device geometry high mobility materials are used in at least two-dimensional structures which motivates the estimation of transport parameters to realize a device simulation with a comprehensive model for e.g. the extended Gaussian disorder model (EGDM)[5].

Due to the strong temperature dependence of the charge carriers mobility, a quantitative analysis of the current-voltage characteristics of organic devices requires the knowledge of the temperature in the organic layers and the simulation of the heat flow from the circuit into the surrounding materials [6]. Therefore, model devices with particularly large power dissipation may help to elucidate the impact of Joule heating on the mobility of the charge carriers and the resulting device performance.

In the present work, we investigate a vertical layer sequence consisting of n-doped/intrinsic/n-doped (nin) C_{60}. The particularly high electron mobility in C_{60} and the thermal stability allows to study the temperature dependence of this device up to about 200°C before eventually reaching thermal breakdown. The enhanced mobility at elevated temperature represents a positive feedback mechanism, resulting in a highly nonlinear current-voltage characteristic already at rather moderate driving voltages. In the remaining part of this work, we will demonstrate that this nonlinearity can be related to a strong heating of the device proportional to the dissipated electrical power.

In Sec. 2, a simple analysis of the EGDM reveals that the device temperature rising with the power dissipation represents a positive feedback mechanism for the mobility of the charge carriers, the current density and the electrical power. As explained in Sec. 3 in more detail, these considerations have allowed us to design a model device where the impact of temperature on the current-voltage characteristics is particularly pronounced.

Sec. 4 is devoted to the electrical characterization of this device, revealing substantial changes of the IV characteristic beyond a power per area of about $10\,\mathrm{W/cm^2}$. In Sec. 5, analytical approximations and numerical simulations of the heat conduction from the whole device into the environment are presented. Sec. 6 is devoted to infrared camera measurements of the device, demonstrating unambiguously that the currents near the contact edges results in additional heat sources superimposed to an approximately homogeneous Joule heating arising from the entire area of the active device. The thermal breakdown is directly related to the heating at the edges, as shown in Sec. 7. The paper is concluded in Sec. 8.

2. Positive feedback

For small area devices grown on substrates with high thermal conductivity, it was demonstrated that organic materials can withstand extremely high current densities up to $1\,\mathrm{MA/cm^2}$ [7, 8]. Similar structures were produced to build fast organic rectifying diodes, and the efficient heat flow through the highly thermal conductive substrate was identified as a key ingredient to prevent breakdown [9]. Whereas heat conduction in OLEDs operated at much lower power and temperature was investigated in some detail [6], similar studies of the heating effects in high power devices with small active areas are missing.

In inorganic semiconductors relying on band transport, under ambient conditions phonon scattering will lead to a lowering of the mobility μ with rising temperature following the relation

$$\mu(T) \propto T^{-n} \,, \tag{1}$$

where the exponent n varies from $\frac{1}{2}$ to $\frac{3}{2}$ depending on the dominating type of electron-phonon interaction [10]. Except for highly purified materials in crystalline order[11, 12], charge transport through organic materials does not rely on the electronic energy band structure in k-space. Instead, most of the organic semiconductors feature hopping processes between adjacent molecules, with hopping rates governed by the Miller-Abraham law [13]. In combination with a normally distributed state density, Bässler has developed the Gaussian disorder model (GDM) relying on Monte Carlo simulations [14]. As a result, for a Gaussian density of states (DOS)

$$\mathrm{DOS}(E) = \frac{N_t}{\sqrt{2\pi}\sigma} \exp\left(-\frac{(E-E_0)^2}{2\sigma^2}\right) \tag{2}$$

of width σ and site density N_t, the temperature dependence of the mobility at low charge density can be obtained from the relationship

$$\mu(T) = \mu_0 \exp\left(-c\frac{\sigma^2}{(k_\mathrm{B}T)^2}\right) \tag{3}$$

where c is a constant of the order of $c \approx 0.4$, resulting in a monotonous increase of the mobility with temperature, $d\mu/dT > 0$ [14]. Subsequent extensions of this approach have revealed that at high charge carrier densities, an additional dependence of the mobility on density results in a rise of the mobility according to

$$\mu(T,n) = \mu_0 \exp\left(-c\frac{\sigma^2}{(k_\mathrm{B}T)^2}\right) g_1(T,n) \tag{4}$$

where the function $g_1(T, n)$ is monotonously increasing with density for sufficiently large Gaussian DOS, $\partial g_1/\partial n > 0$ [15, 5].

As a consequence of this so-called extended Gaussian disorder model (EGDM), there are two positive feedback mechanisms. First, similarly to the previous GDM model, the mobility is growing for rising temperature, $\partial\mu/\partial T > 0$, so that the Joule heating of the device results in an increase of the current density $j = en\mu E$ via the larger mobility. This is in sharp contrast to the behaviour of inorganic semiconductors at ambient temperature, where $\partial\mu/\partial T < 0$ results in a stabilization of the current density via a negative feedback mechanism. Second, in an nin device, a rising temperature will smear out the equilibrium distribution of the electron density, so that the density minimum in the intrinsic layer will also rise. This enhanced electron density n in the intrinsic region will increase the conductance $j/E = en\mu$, and the positive slope $\partial\mu/\partial n > 0$ will enhance the conductance of the intrinsic layer even further via the mobility rising with the larger density.

In summary, Joule heating of an nin device will increase the electron mobility everywhere in the circuit, and the electron density around its minimum near the center of the intrinsic layer. Both mechanisms contribute to an increased conductance in all regions of the device, including in particular the central part of the intrinsic region. As a consequence the series resistance of the organic circuit will decrease with rising temperature.

3. Device design

As large injection barriers between the contacts and the adjacent organic layers would spoil the performance of the entire device, the reduction of these barriers via doping of the organic layers has proven to be a particularly successful strategy, resulting in essentially Ohmic injection [16]. Therefore, it has become common practice to dope the organic layers adjacent to the contacts in order to reduce the driving voltage.

In previous applications of the EGDM model to OLEDs, the determination of the energy offsets between the transport levels in different layers constituted a major challenge. For nin and p-doped/intrinsic/p-doped (pip) model devices resembling the layer sequence of an OLED, it was shown that ultraviolet photoelectron spectroscopy (UPS) can serve as a guideline for both the width of the Gaussian DOS and for the energy offsets at organic-organic interfaces. On the basis of these parameters derived from UPS, one-dimensional simulations of the charge transport with the EGDM model agree well with the measured IV characteristics [17].

For the rather low mobilities in the materials used in OLEDs, the temperature dependence of the IV characteristics and the series resistance of the transparent contact result in a disturbing inhomogeneity of the emission intensity. Due to the sensitivity of the phosphorescent emitters to elevated temperatures, the main challenge consists in a minimization of the thermal stress. As a consequence, OLEDs are not suitable for fundamental studies of changes of the charge carrier mobility over a wider range of temperatures.

In the case of OFETs or fast rectifying organic diodes, high mobility materials are employed to achieve the highest possible switching speed. For building nin devices with such materials, an active area larger than $0.1\,\mathrm{mm}^2$ is not suitable since this will lead to a low device resistance of the order of the preresistance or even less. Thus, an active area as small as $200\,\mu\mathrm{m} \times 200\,\mu\mathrm{m}$ is preferred, still within reach of a normal shadow mask system where the device is defined by the overlap of two crossbar electrodes. This setup is typically applied for creation of fast rectifying organic diodes which can be used for RFID technology [9].

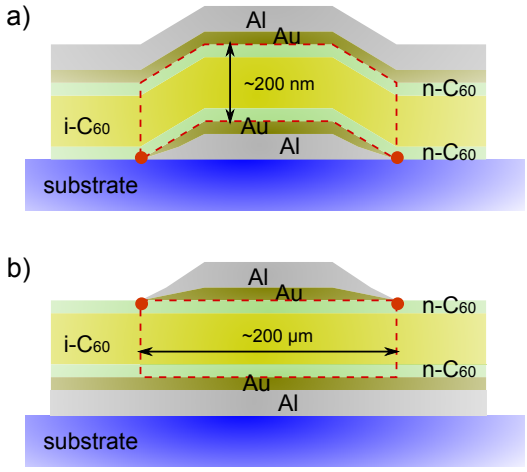

FIGURE 1. Schematic structure of the device and cross-sections along a) top contact and b) bottom contact. For simulating the heat conduction, we use a volume heat source (within red dashed line). Heat sources localized along lines oriented perpendicular to the picture are indicated by red dots. The arrows indicate the typical dimensions of length and height. The small angle of the trapezoidal electrodes is below 1° and does not affect the effective thickness of the organic semiconductor layer. For further geometric details compare Appendix A.1.

Another reason to downscale the device is that the high frequency properties are not only governed by the mobility, but also by the RC time of the system. For a quadratic active area, the capacitance will scale proportionally to the squared edge length d, $C \propto d^2$. At the same time, the resistance of the electrode will only scale inverse proportionally to d, $R \propto d^{-1}$. Thus, downscaling improves the high frequency capabilities according to a reduced RC time $\tau = RC \propto d$, so that operation above 100 MHz has become possible [18].

The smallness of such a structure underlines the need to investigate the lateral uniformity of current transport. One has to clarify whether they are still understandable in an one-dimensional transport model which would guarantee an easy parameter extraction. Furthermore, at high current densities, heat transport from the electronic circuit into the surrounding material, characterized by the thermal resistance, plays a major role for understanding the limits of operation.

4. Experimental results

As test structures, we use nin devices with an intrinsic layer sandwiched between two n-doped layers adjacent to the metal contacts (cf. Fig 1). The thickness of the central intrinsic layer is varied from 100 nm to 400 nm, with the thicknesses of the n-doped layers kept fixed at 20 nm. The resulting sequence of layers is embedded between two metal electrodes using a combination of Al (> 200 nm) and Au (20 nm). The thick Al electrodes are important to keep the series resistance as low as possible, and the additional Au shall prevent the oxidation of the aluminum by residual oxygen or water in the nitrogen atmosphere of the encapsulated samples [19]. This layer sequence guarantees identical injection conditions at the gold/organic interfaces and and a vanishing built-in voltage.

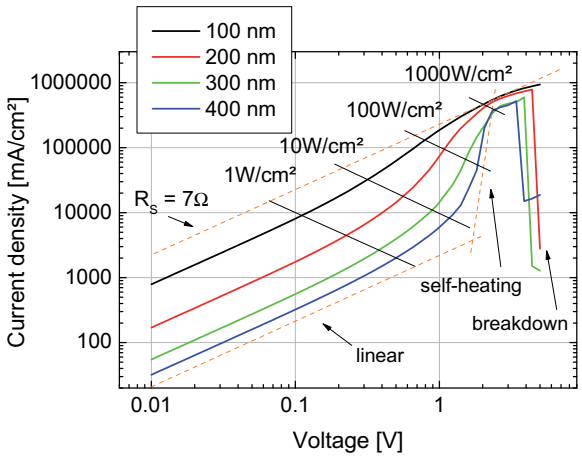

FIGURE 2. IV characteristic of an nin device comprising C_{60} for various intrinsic layer thicknesses. Above power densities of $10\,W/cm^2$ the current densities increase rapidly due to Joule self-heating, only limited by a series resistance of around $7\,\Omega$. Breakdown appears at around 3 V to 5 V.

The samples are produced on glass substrates (Borofloat 33, Schott AG[1]) using thermal vapor deposition. We employ C_{60} as n-type organic semiconductor with mobilities in the range above $0.1\,cm^2/Vs$, ensuring high current densities at moderate driving voltages [18, 20]. Doping of C_{60} is realized by coevaporation with tungsten paddlewheel $W_2(hpp)_4$ at a doping concentration of 2wt% [21, 22].

Structuring of the device is done by shadow masks, which originally were designed for active areas of $200\,\mu m \times 200\,\mu m$. Albeit, due to the configuration of substrate, shadow mask and evaporator, slightly larger electrode widths are measured using a profilometer (see Appendix A.1). Thus, the active area is about $0.06\,mm^2$ instead of the nominal design size of $0.04\,mm^2$, and the electrodes have a typically trapezoidal shape [23] as schematically visualized in Fig. 1. The angle between the side and the baseline of the trapezoid is in a range below 1°. But nevertheless, we can assume a constant thickness of the organic material within the active area.

The electrical characterization is performed using a Keithley 2400 SourceMeter measuring 50 points of voltages in logarithmic order with no delay or stop time between consecutive voltages. The IV curves of the device are shown in Fig. 2 for various thicknesses of the intrinsic C_{60} (i-C_{60}) layer. The potentials applied to the electrodes lead to an electron flow from the top to the bottom electrode. As expected the current density reaches very high values up to $10^6\,mA/cm^2$, mainly due to the high mobility of C_{60}. In literature, even higher current densities are published, demonstrating that organic semiconductors sustain quite high charge carrier concentrations [8]. With increasing i-layer thickness the current densities are decreasing. A similar behavior and comparable current densities are measured with reversed bias, indicating symmetric injection and transport properties (see Appendix A.2). Thus, we can assume that the electrical potential within the device is not influenced by a built-in potential.

In the voltage regime below 0.5 V, the current-voltage dependence follows a linear potential law as expected for an Ohmic injection. At higher voltages above 0.5 V,

[1]product sheet: http://www.schott.com/borofloat

a strong increase of current can be measured, especially for samples with higher intrinsic layer thicknesses. This shoot up can be assigned to Joule self-heating occurring in organic semiconductors under higher current densities in equilibrium with the heat conduction through the substrate [8, 24]. A infrared camera picture of the sample in the self-heating regime at a voltage of 2 V is presented in Sec. 6. In comparison, we obtain no measurable temperature increase in the linear regime. In Fig. 2, additional lines of constant power density support the correlation between heating and the IV characteristic.

More than the voltage, the incorporated power density gives a threshold between a constant temperature and a self-heating regime. Above $10\,\mathrm{W/cm^2}$, a strong influence of heating is obtained, especially for samples with an intrinsic layer thickness of 300 nm and more. This difference between the samples originates from a series resistor (excluding device resistance) of the setup around $7\,\Omega$, determined by the asymptotics of the curves at the highest current densities. Since the thickest device has the highest resistance, the current shoot up at voltages above $1\,V$ can be observed best, and a power law $j \propto U^{\alpha}$ with an exponent $\alpha > 10$ is necessary to describe the data. For devices with lower thicknesses, smaller power laws can be obtained due to the stronger influence of the series resistor, e.g $\alpha \approx 4$ for $\mathrm{d} = 200\,\mathrm{nm}$ (cf. Fig. 2). This impact of the series resistor has to be considered when IV curves are analyzed to calculate parameters, e.g mobility. Finally, the breakdown of the device appears between 3 V and 5 V due to self-heating. Our measurement shows a slightly earlier collapse of the device using 400 nm of i-C_{60}, assigned to the fact that a thicker device needs a higher temperature rise due to self-heating to reduce its resistance to a value of the order of the series resistor.

All previous discussions take into account that organic semiconductors tend to increase their mobility with increasing temperature as mentioned in Sec. 2. As a consequence, self-heating will increase the mobility of the molecular layer, affecting in turn the current density. The resulting power density will again boost the Joule self-heating and induces a positive feedback effect. Therefore, we predict a feedback mechanism which is the reason for the observed overshoot of current density. According to the EGDM model, the constant c in Eqs. (3) and (4) assumes similar values different organic materials, so that the variance σ^2 of the Gaussian DOS in Eq. (2) will give the strongest positive temperature feedback.

5. Numerical simulation and analytical estimates of heat transfer

In contrast to the situation of OLEDs or OSCs, in our case the thickness of the substrate is larger than the edge length of the active area. Therefore, we cannot confine the analysis to a one-dimensional (1D) approximation and have to consider the heat transfer as a full three-dimensional (3D) problem. The heat conduction is described by Fourier's law

$$q = -\lambda \nabla T, \tag{5}$$

where q denotes the heat flux, λ represents the heat conductivity, and ∇T the temperature gradient.

For a first glance on the heat transfer from the active region to the boundary of the device we study the heat transfer through a half hollow sphere. The dissipated heat power $\dot{Q}$ is supplied over the inner boundary of the sphere Γ_s with radius R of the hollow sphere and transported to the outer boundary Γ_r, see inset of Fig. 5 (solid blue and grey dotted boundaries, respectively, where we show only one half of the cross-section due to symmetry). The temperature distribution is spherically

TABLE 1. Material database

Material	Heat Conductivity $[Wm^{-1}K^{-1}]$
Borofloat33	1.2
aluminum	236
air	0.0261
encapsulation glass	0.76
C_{60}	0.4

symmetric and depends only on the distance r to the origin. The heat flux fulfills

$$q(r) = \frac{\dot{Q}}{2\pi r^2} = -\lambda \frac{d}{dr} T(r), \tag{6}$$

leading to the well-known $1/r$ temperature profile

$$T_1(r) = \frac{T_s R}{r}, \quad T_s = \frac{\dot{Q}}{2\pi\lambda R}, \tag{7}$$

where T_s represents the constant temperature on Γ_s. This approach realizes the correct far-field behavior of the temperature distribution, but fails to describe the heat transport in and near the active region. We attack this problem by full 3D simulations of the crossbar structure, in particular taking into account the spatial variation of the heat conductivity. These results are compared to analytically solvable models for simplified geometries.

5.1. **3D simulation of heat transport.** We study the stationary heat conduction around the crossbar structure due to Joule heating in the active area by calculating a 3D numerical solution on the spatial domain $\Omega = [-L, L] \times [-L, L] \times [-H_{\text{sub}}, H_{\text{caps}}]$,

$$\nabla \cdot q = -\nabla \cdot (\lambda(x) \nabla T(x)) = f(x) \quad \text{in} \quad \Omega, \tag{8}$$

with the heat source $f(x)$ and the boundary conditions

$$-\nu \cdot q = \nu \cdot (\lambda(x) \nabla T(x)) = \kappa(x)(T(x) - T_0) \text{ on } \partial\Omega, \tag{9}$$

where ν denotes the outer normal vector, λ represents the spatial profile of the heat conductivity defined by the device structure, see Tab. 1, κ means the heat transfer coefficient, and T_0 is the ambient temperature around the device. For the simulations the half length L is chosen to 2 mm, the height of the substrate glass H_{sub} is 1.1 mm and the position of the top of the encapsulation glass H_{caps} is around 1.1 mm. The ambient temperature T_0 is assumed to be 293 K.

Due to the symmetry it is sufficient to simulate only a quarter of the crossbar structure using symmetry boundary conditions at the cross-sections. For simplicity we used contact stripes with equal width (245 μm) and rectangular cross-sections instead of the trapezoidal ones, see Fig. 1. The width of the contacts is chosen in such a way that the crossing area is of the same size as the real one. Furthermore, as electrode material we used pure aluminum.

For the numerical solution and visualization we created a code based on the toolbox `pdelib` [25] developed and maintained at WIAS. The spatial discretization is based on a Voronoi box finite volume scheme which features global and local heat conservation and guarantees that the numerical solution remains within the a priori bounds of the solution of the continuous problem Eq. (8) [26].

Since the lateral dimensions ($\sim$100 μm) of the electrically driven heat source are 1000 times larger than vertical dimensions ($\sim$100 nm), the structure is highly anisotropic. A series of tensor product meshes of different refinement levels is used for computation. Each of these meshes exactly reproduces an approximation of the device geometry by anisotropic cuboids. The strong anisotropy leads to large

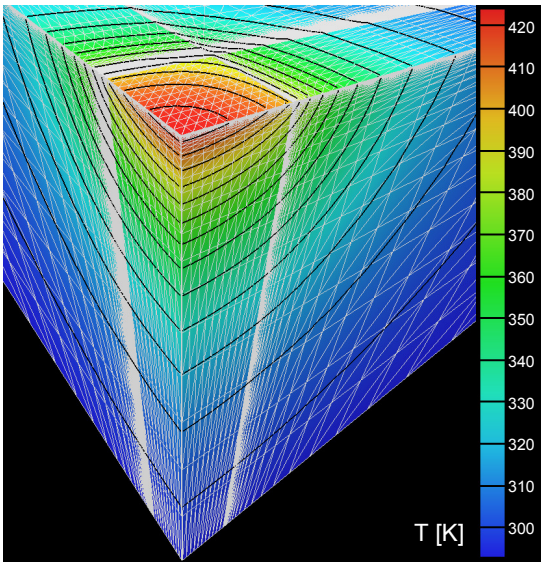

FIGURE 3. Computed 3D temperature distribution in the glass substrate and crossbar structure. The dissipative power of 0.1 W is supplied homogeneously in the active region. The height of the object equals the substrate thickness.

condition numbers of the linear system of equations arising from the discretization of Eq. (8). An iterative strategy around the sparse direct solver PARDISO [27, 28] combined with time embedding ensures that the correct solution is obtained.

First, the simulation code was validated by the solution for the hollow sphere problem, see Eq. (7), and by further analytically solvable models introduced later. Based on these models, the refinement strategy for the computational grids used for the simulation of the full device structure has been chosen. The computational grid has to be fine near to the active region, whereas a coarser mesh can be used to resolve the surrounding part adapted to the $1/r$ behavior of the temperature.

We studied Joule heating by a homogenous heat source in the active area (cf. Fig. 1), as expected for our nin test structure for one-dimensional current transport. The simulation, shown in Fig. 3, allows for a detailed view on the temperature distribution. In this perspective 3D view, we see 1/8 of the complete volume and the thickness of the object equals exactly the substrate glass. The white grid shows a thinned mesh of the real mesh we used for the computations which is most dense in the active region. Additionally, it is also finer at the electrode edges for resolving the material interfaces. The temperature profile, indicated by black lines with a distance of 10 K, reveals the transition from a more planar-like distribution due to the planar shape of the heat source to the typical spherical solution $T \propto 1/r$ as given by Eq. (7). Due to the higher heat conductivity of glass with respect to air, the essential part of the heat transport occurs through the substrate.

The heat transported laterally by the contacts does not cool the device sufficiently. However, due to the extremely high heat conductivity of the metal and the small thickness of the contacts, in perpendicular direction the temperature difference across the metal films is negligible. Thus, the temperature on the surface of the contacts coincides with the temperature of the active C_{60} layer at the interface between contact and C_{60}.

This behavior can be studied in more detail by cross-sections in xy-plane in the center of the heat source (Fig. 4a) and in xz-plane (Fig. 4c). In particular,

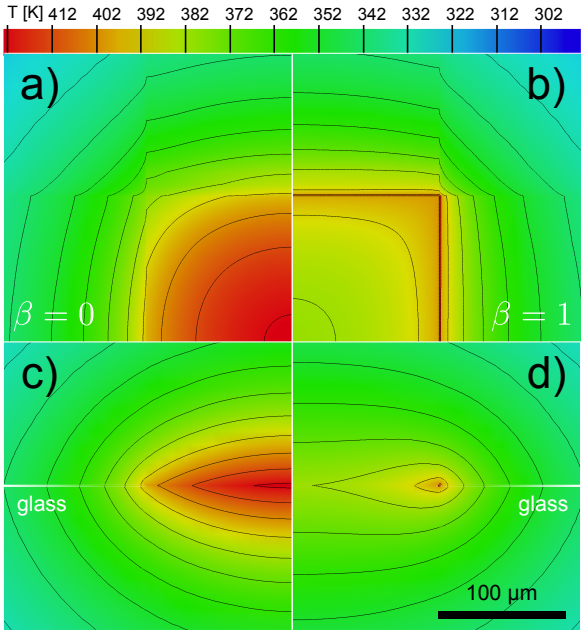

FIGURE 4. Cross-sections of computed 3D temperature distributions for dissipative power of 0.1 W. Lateral cross-section for heat supply (a) homogeneous in active region $\beta = 0$, and (b) concentrated at the edges of the electrodes $\beta = 1$, see red-dashed region and bullets in Fig. 1, respectively. Both pictures are taken halfway through the i-C_{60} layer. Vertical cross-section corresponding to homogeneous heat supply (c) and at edges (d).

one observes as an characteristic feature circular isolines within the active region. Additionally, far away from the active region an isotropic behavior can be found, see Fig. 3. That suggests to describe the temperature distribution by analytical models for the heat transfer.

5.2. **Detailed analytical approach.** Motivated by the observation of the circular structure of the lateral temperature profile in the active region, see Fig. 4a, we consider the heat transfer from a thin circular disc into a thick substrate material. The substrate material is modeled by an infinite half space and the heat source is represented by a boundary condition describing a constant heat flux $q = \dot{Q}/(\pi R^2)$ on a circular disc with radius R. In the inset of Fig. 5 the position of this disc is represented by the boundary Γ_{d}. On the remaining part Γ_{N} of the boundary we suppose no-flux boundary conditions. The analytical solution for that problem given in [29, p. 216] results in an axially symmetric temperature distribution $T = T(r_{\parallel}, z)$ with $r_{\parallel} = \sqrt{x^2 + y^2}$. On the symmetry axis, an analytical expression for the temperature distribution $T_2(z) = T(r_{\parallel} = 0, z)$ can be derived

$$T_2(z) = T_0 + \frac{T_{d,max}}{R}\left(\sqrt{R^2 + z^2} - z\right), \qquad \text{with} \quad \mathrm{T_{d,max}} = \frac{\dot{\mathrm{Q}}}{\pi\lambda \mathrm{R}}. \tag{10}$$

The temperature profile $T_2(z)$ on the symmetry axis is shown in Fig. 5. The temperature across the area of the heat supply Γ_{d} varies in a similar way as that for numerical simulation of the full problem. Its minimum attained at the boundary

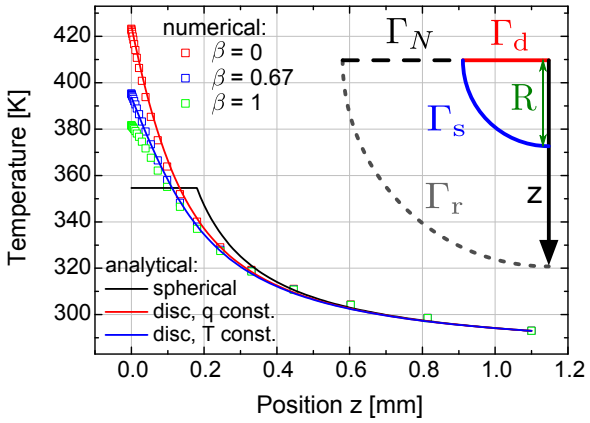

FIGURE 5. Temperature profile in the substrate material along the symmetry axis for different analytical models with dissipative power of 0.1 W and radius $R = 185.5$ μm. Analytical solutions for a) constant temperature on half sphere surface Γ_s (black solid) b) constant heat flux through a disc Γ_d (red solid) c) constant temperature on a disc Γ_d (blue solid) are shown, respectively. The numerically computed temperatures along the symmetry axis are indicated by square symbols. Homogeneous heat supply in the active region corresponds to $\beta = 0$, whereas $\beta = 1$ means heat sources concentrated at the edges. Inset: geometrical setting for the different analytical approaches with hollow sphere Γ_s of radius R, and circular disc Γ_d of radius R, and boundary Γ_N surrounding the disc Γ_d.

of Γ_d is given by

$$T_{d,min} = \frac{2\dot{Q}}{\pi^2 \lambda R} = \frac{2}{\pi} T_{d,max}. \tag{11}$$

The ratio $T_{d,\min}/T_{d,\max} = 2/\pi \approx 64\%$ compares well to a temperature decay of 35% between the center and the edge of the quadratic heat source obtained by the numerical simulation, see Fig. 4a. For details of the derivation see Appendix C.1.

5.3. **Thermal resistance.** The application of the analytic model to our problem raises the question how to choose the radius R describing the circular heat source in order to reach agreement between Eq. (10) with the simulation results, since the simulated active area is a square described by the contact width L_0.

For fitting of the analytic solution to the computed results we select the thermal resistance $\Theta_{\rm th}$ defined by

$$\Theta_{\rm th} = \frac{\Delta T}{\dot{Q}} = \frac{T_{\rm ref} - T_0}{\dot{Q}}. \tag{12}$$

It is a property of the complete device consisting of electrical circuit, substrate and encapsulation glass characterizing the temperature rise at specific points within the electrically active region with respect to the ambient temperature.

The analytical models introduced, lead to different temperature profiles, but the expressions Eqs. (7), (10)-(11) for the temperature at specifically chosen reference points on the heating boundary, see Tab. 2, have the same formal structure. These expressions differ only by a problem-dependent geometry factor C given in Tab. 2. Additionally, the far-field temperature profiles on the symmetry axis coincide with

problem and boundary conditions	reference temp. T_{ref}	geo. factor C
half sphere, $\dot{q} = \text{const}$	$T_s = \text{const}$ on Γ_{s}	1
disc, $\dot{q} = \text{const}$	$T_{d,\max} = T(0,0)$	2
disc, $\dot{q} = \text{const}$	$T_{d,\min} = T(R,0)$	$\frac{4}{\pi}$
disc, $T = \text{const}$	$T_d = \text{const}$ on Γ_{d}	$\frac{\pi}{2}$

TABLE 2. Geometric factors and reference temperatures for different analytical approaches, see Eqs. (7), (10)-(11), and (16).

the $1/r$ solution for the hollow sphere (7), see Fig. 5. As a result we end up with a general expression for the thermal resistance given by

$$\Delta T = T_{\mathrm{ref}} - T_{\mathrm{far}}(z) = \frac{1}{2\pi\lambda}\left(\frac{C}{R} - \frac{1}{z}\right)\dot{Q} = \Theta_{\mathrm{th}}\dot{Q}. \tag{13}$$

In particular, the thermal resistance is inversely proportional to the substrate heat conductivity λ and can easily estimated for various substrate materials. For organic vertical devices surrounded by glass and air, the total thermal resistance Θ_{th} can be estimated by two half-space problems in parallel connection by

$$\frac{1}{\Theta_{\mathrm{th}}} = \frac{1}{\Theta_{\mathrm{th,glass}}} + \frac{1}{\Theta_{\mathrm{th,air}}}. \tag{14}$$

A good agreement between the analytically derived thermal resistance Eq. (13) and the simulation was obtained by using

$$R = \alpha\frac{L_0}{2} + \Delta R \tag{15}$$

with $\alpha = 1.208$ and $\Delta R = 37\,\mu$m for crossbar structures with contact width L_0 ranging from 150 μm to 350 μm, see Fig. B.2 in Appendix B.2. The scaling factor α describing the length conversion from square to disc lies between values for area preserving ($\alpha = 1.128$) and perimeter preserving ($\alpha = 1.28$) conversion. The shift ΔR describes the enlargement of the active area by lateral heat flow guided by the highly conductive electrode stripes. For the analytical expression we used $z = H_{\mathrm{sub}}$, $T_{\mathrm{ref}} = T_{\mathrm{d,max}}$ and $C = 2$. Please note that this fit is only possible for device geometries with sufficiently large substrate thicknesses, $H_{\mathrm{sub}} > 3R$.

The conversion formula gives $R = 185.5\ \mu$m as the effective radius for the crossbar structure ($L_0 = 245\ \mu$m) under investigation. We compared the analytical temperature profile on the symmetry axis Eq. (10) to the one obtained by the numerical solution of the full problem, see Fig. 5 (red curve and squares, respectively). The results are in excellent agreement. For the points of distances $r > 3R$, all temperature profiles exhibit the usual $1/r$ asymptotics.

5.4. **Isothermal heat supply by a circular disc.** Furthermore, we investigated the heat supply over a disc with constant temperature T_d on Γ_{d}. Again, the resulting temperature distribution is axially symmetric and its values on the symmetry axis $T_3(z) = T(r_{\parallel} = 0, z)$ have the form [29, p. 215]

$$T_3(z) = T_0 + \frac{2T_d}{\pi}\arcsin\frac{R}{\sqrt{R^2+z^2}}, \quad T_d = \frac{\dot{Q}}{4\lambda R}. \tag{16}$$

The temperature profile is shown in Fig. 5. Also this case can be fitted with the analytical expression (13) derived for the thermal resistance, provided that $C = \frac{\pi}{2}$, see Tab. 2. For further details see Appendix C.2.

6. Comparison between experimental results and simulation

The analytical approach as well as the simulation provide detailed insight into the heat transport away from the electrically driven heat source. In this section, we try to validate these results by thermal imaging of the test structure.

6.1. **Thermal imaging of the test structure.** We use an IR camera VarioTHERM head II (company: JENOPTIK AG) with a macro lens to image the device under bias stress (cf. Fig. 6). To avoid measuring IR radiation emitted by the camera and reflected by the sample, the camera is tilted by a small angle with respect to the sample normal. Before the measurement, we calibrate the camera regarding the Al electrode of the sample in a temperature range around 340 K. Since the resulting calibration factor is applied to the whole picture, the temperature values in areas containing exclusively C_{60} are not correct. A calibration for C_{60} is not practicable due its high transparency in the IR region. Still, this property can be used to assume that the electrodes beneath and on top of the C_{60} layer have the same emission spectra, so that the IR camera determines equal temperatures for both types of contacts. Therefore, no distinction between bottom and top contact is necessary (see Appendix A.5). As shown in the simulations, the vertical heat transport within the contacts of the device is very efficient, and consequently, the electrodes reveal the temperature of the device. Measurements are performed from the top view (through encapsulation glass, Fig. 6a) and from the bottom view (through substrate glass, Fig. 6c), allowing us to examine differences between both sides of the device. For experiment and simulation, a device with 300 nm i-C_{60} layer thickness has been used.

In Fig. 6, the strong heating effect is clearly visible. Below 0.3 V, no temperature rise is obtained in accordance to the IV curves. Independently of the voltage polarity, the qualitative appearance of the thermo picture remains the same. Therefore, we measure at a voltage of 2 V for both cases, top and bottom view. One difference between these measurement configurations is the shape of the temperature distribution in the regions with no electrodes. For top view a convex shape and for bottom view a concave shape is obtained. We explain this by the different configurations between both aspects. On the top side, there is a 0.6 mm thick encapsulation and a spacing of around 0.5 mm to the device. The bottom side consists of a 1.1 mm thick substrate glass without any spacing between the device and the glass. Since the calibration is only done for Al, all areas without any metal electrodes appear hotter or cooler if their real emission coefficient is higher or lower than the one of aluminum. Furthermore and most relevantly, the substrate glass heats up during operation, in contrast to the encapsulation glass. Using even higher voltages of up to 3 V, we finally reach temperatures above 473 K (200°C) in the center of the active area.

Assuming an equal power dissipation within the device (cf. Fig. 1) the 3-dimensional heat transport simulation shows a global maximum in the center of the active area (cf. Fig. 4a) and c)). Also the analytical solution for a constant heat dissipation within a circular disc (Eq. (10)) reproduces this behavior. In contradiction to these results, thermal imaging reveals the strongest heating at the edges of our test structure. Most interestingly, only two edges of the device are visible in the IR picture, but dependent on the direction of the view, they alter from vertical to horizontal orientation in Fig. 6a) and c). In both pictures the vertically aligned electrode remains the top electrode, and thus, we conclude that all the four edges heat up, but only two of them are visible from one side. These edges are exactly those which are not hidden by an aluminum electrode towards the infrared camera. This result is again independent from the voltage polarity.

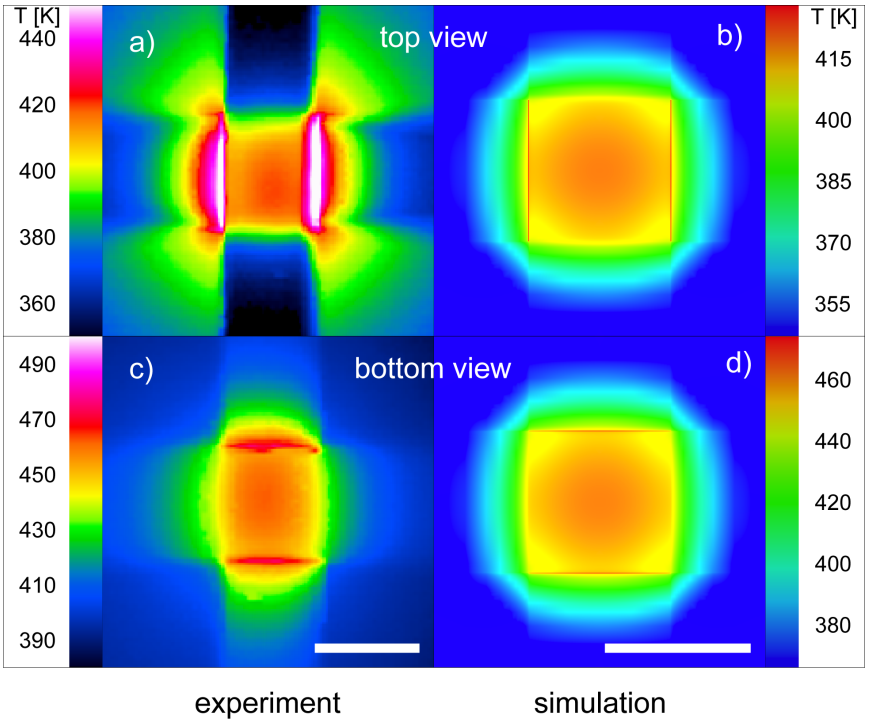

FIGURE 6. Comparison of experimental results and simulation. Measurements were performed from different directions, where top view means through the encapsulation glass and bottom view through the substrate glass. For the top view a) and b) the vertical electrode is closer to the camera, analogue the horizontal electrode for the bottom view c) and d). Additional line heat sources in the simulation are necessary to rebuild the experimental results. Both, experiment and simulation are done for a device with 300 nm i-C_{60} layer at a voltage of 2 V. For simulation we use 0.115 W and 0.155 W for top and bottom view, respectively to achieve equal temperatures in the center of the active area with respect to the experimental results. The scale bar represents the width of the active area (245 μm). Further details can be found in Appendix A.6.

As shown in Fig. 1 the profile of the electrodes is trapezoidal with small angles at the lateral boundaries. Since the electrical field typically concentrates at those edges, the current density will be enhanced there. Moreover, we assume that even parts of the electrodes not belonging to the active area will inject charge carriers into the organic layers and contribute to the current transport. Furthermore, the thickness of the metal electrode is thinnest at the edges. Consequently, the sheet resistance of the electrode increases. This leads to higher power dissipation accompanied by a decrease of the heat transfer capabilities promoting the further heat up at the edges. Also, the influence of the doped layer has to be considered. The conductivity of C_{60} doped with $W_2(hpp)_4$ reaches up to 4 S/cm, while undoped C_{60}-layers have a conductivity in the range of 10^{-8} S/cm [22, 30]. This extreme difference in conductivity supports the in-plane current transport of the n-C_{60} layer. At the same time, the injection as well as the vertical electrical conductivity are also improved. With increasing i-C_{60} layer thickness, we estimate a proportionally

higher contribution of the lateral current transport. Thus, doped layers can ensure sufficient injection properties for characterization of transport parameters, but they modify the structure into a 3-dimensional system, where at least the current density near the edges can no more be assumed to occur exclusively homogenous between the electrodes.

6.2. **Comparison with simulation.** In further 3-dimensional heat transport simulations we try to reproduce the experimental results qualitatively. This is possible by assuming additional heat sources localized at the edges of the electrodes within the active area slightly shifted towards the organic layers, as visualized with red bullets in Fig. 1. Consequently, the associated heat conductivity is attributed to C_{60}. This step is motivated by the power which will mostly dissipate in the molecular layer due to the enhanced charge carrier concentration and the electrical field. The pure influence of such line heat sources on the device temperature can be seen in Fig. 4b) and d). In contrast to the case of the volume heat source studied in Sec. 5.1, we obtain a pronounced temperature maximum at the heated edges, whereas in the active region the temperature variation is relatively small.

Although these heat sources are discrete, the temperature distribution is quite homogeneous, caused by the large ratio of substrate thickness to device side length. To describe a mixture of an equally distributed power dissipation and line heat sources, we introduce the factor β describing the part of the power assigned to the edges. Under the assumption that the heat conductivity λ is independent on the temperature, the solutions of both cases can be added linearly. Thus, the result is a linear combination of Fig. 4a) and b).

At $\beta \approx 0.67$, the temperature distribution in the center of the active area changes from a local maximum to a local minimum. Besides the edges of the active area, a very uniform temperature distribution is then obtained (see Appendix B.1). In this case the analytical approach for a circular disc with constant temperature (section 5.4) can be applied. The temperatures along the z-axis coincide well with the simulation (cf. Fig. 5) if we again use the same effective disc radius $R = 185\,\mu m$ obtained by Eq. (15). Below a value of $\beta \approx 0.25$ the global temperature maximum is attained in the center of the active area as predicted by an equally distributed heat source ($\beta = 0$).

The best representation of the experimental results is achieved using a factor $\beta = 0.5$ for the simulation, as shown in Fig. 6. This value must lie between 0.25 and 0.67, since we have a global maximum at the edges, but also a local maximum in the center of the active area. Most interestingly, although four line heat sources are incorporated, only two of them are again visible. By comparing experiment and simulation for corresponding views, we find a nearly perfect accordance. Therefore, the explanation of this effect can be now easily given by the simulation. In Fig. 4b, the cross-section is exactly taken in between the electrodes (halfway through the i-C_{60} layer). The impact of all four line heat sources can be observed. But if we take the cross-section along the outer surface of the electrodes, as shown in Fig. 6b) and d), similar to the visible regions in Fig. 6 a) and c), only the line heat sources which are close to the investigated electrode can be seen through. The other two line heat sources are smeared out by the C_{60} and the metal electrode.

The effect of smearing out the heat source can also be observed elsewhere. The lateral heat transport of the metal electrode is insufficient to cool down the device efficiently. But in a small range of some ten micrometers, the heat transport of the thin metal film is adequate to broaden the distribution as seen in Fig. 6a) and c). This fact is also reflected by Eq. (15), where one has to consider an effective radius R of the circular disc with a constant enlargement of $\Delta R = 37\,\mu m$ within the analytical approach.

6.3. **Estimation of thermal resistance.** In Fig. 6 we have to use lower dissipative power in the simulation to achieve a similar temperature range as in the experiment. The temperature rise of the device with respect to the dissipated power is characterized by the thermal resistance Θ_{th} given in Eq. (12) in the center of the active area. Since the analytical approach is adjusted to the simulations by the effective radius R, indicated by equal temperatures at z = 0 in Fig. 5, both approaches deliver equal values for the thermal resistance. Using Eq. (13) and Tab. 2 the thermal resistance can easily be estimated by taking an effective radius into account (cf. Eq. (15)). In the case of constant heat distribution ($\beta = 0$), the thermal resistance is $\Theta_{\mathrm{th}} = 1300\,\mathrm{K/W}$, whereas for the case of constant temperature distribution ($\beta = 0.67$), the thermal resistance is $\Theta_{\mathrm{th}} = 1000\,\mathrm{K/W}$. Due to the superposition of solutions of the heat equation, the result for $\beta = 0.5$ as used for comparison with the experiment (cf. Fig. 6) can be calculated by the previously discussed cases. In detail, the simulation reveals $\Theta_{\mathrm{th}} = 1090\,\mathrm{K/W}$ for $\beta = 0.5$ matching the assumption above. This value can be compared with the results obtained by experimental measurements.

For the latter, we determine the temperature at the center of the active area and plot their difference to room temperature with respect to the applied power shown in Fig. 7. The fit of the data reveals a thermal resistance of $\Theta_{\mathrm{th}} = 204\,\mathrm{K/W}$. Due to the heat up, charge carrier density and mobility of the organic semiconductor increase, subsequently decreasing the device resistance below the series resistor of $7\,\Omega$, estimated by the IV characteristic. Therefore, we subtract the part of the power dropping over the series resistor. The fit of the recalculated data exhibits now a Θ_{th} of $755\,\mathrm{K/W}$. With this value we match the correct order of magnitude and the different methods yield consistent results and the analytical approach reproduces the temperature decay into the glass substrate (cf. Fig. 5). Consequently, the high temperatures measured by thermal imaging are verified and from the point of view of the simulation even slightly underestimated.

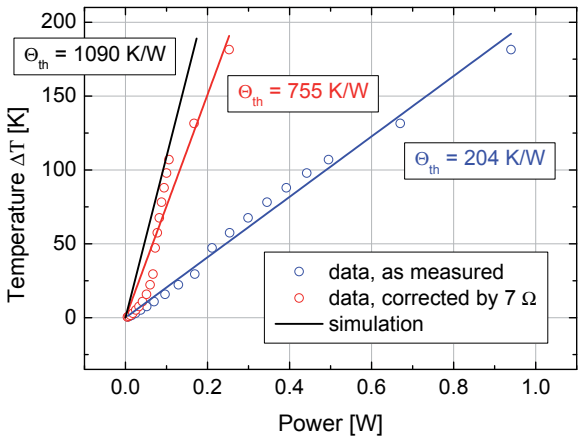

FIGURE 7. The temperature of the devices is measured in the middle of the active area, using the infrared camera. The temperature difference to room temperature is plotted over the applied power. Taking a series resistance of $7\,\Omega$ into account, the fit of the data results into a $\Theta_{\mathrm{th}} = 755\,\mathrm{K/W}$ instead. Thus, the simulated value of $1090\,\mathrm{K/W}$ is in good accordance, showing that the heat transport can be quite well understood by numerical as well as by analytical approaches.

The strong heat dissipation along the edges can be explained considering positive temperature feedback. Once a temperature imbalance in the device is built up, Joule self-heating will even amplify this variations. But due to the fact that the active area is surrounded by line heat sources, a more uniform temperature distribution in the center of the active area is supported, slightly weakening the temperature imbalances. We like to mention further that heating at all edges indicates the impact of all contacts, whether they inject or eject charge carriers. Nevertheless, the highest temperatures are observed at the boundary of the active area, reaching values above 523 K (250°C) at voltages shortly before thermal breakdown appears. Thus, C_{60} is a proper material to combine high current densities at low voltages with an outstanding heat stability, allowing investigations over a wide range of temperatures. As a result, the charge carrier transport in such small active area devices using crossbar electrodes can not be understood as a 1-dimensional configuration. Even without heating, higher current densities at the border of the active area have to be considered.

7. Thermal breakdown of the test structure

To show that edge heating has an influence on the functionality of the operating device we have driven the device to the thermal breakdown. In Fig. 2, the collapse can be seen for higher voltages above 3 V as an abrupt decrease of current density. If the device is subsequently measured a second time, the resistance remains at a high Ohmic level. Thus, an electrical breakdown can be excluded because it would preferably lead to a short. In Fig. 8, a picture of the top contact is shown, recorded with a photocamera mounted onto a microscope. We use only a tonal correction to sharpen the contrast and emphasize the texture of the top contact in the middle of the active area.

The photo reveals the delamination of the top contact at the left side of the active area. On the right side, the deformation has already started at the corners, but is not that progressed. We explain this difference by the fact that the voltage is applied between the left and the bottom electrode and a potential drop in lateral direction within the active area takes already place. Independently on the applied voltage polarity, the top contact breaks always at the edge close to the applied potential electrode. A destruction of the bottom electrode is not observed since this contact is is bound to the glass substrate. Nevertheless, both the top and the bottom side of the active area show edge heating effects, leading to a slightly red shading, indicated by the white arrow. A redeposition of evaporated C_{60} is possible at temperatures above 400°C [31]. Due to the thermal resistance of around 1000 K/W these temperatures can be reached at power densities of 1000 W/cm^2 (cf. Fig 2, but temperatures in this range are not measured by thermal imaging.

Fig. 8 definitely proves the presence of edge heating, initiating the thermal breakdown of the device since the power dissipation will concentrate on a small region of the active area. Consequently, the dissipated power distribution assumed in the simulations seems to be justified. The strip off of the metal contact could be supported by different thermal expansion coefficients of the materials, leading to a deflection. Observed temperature oscillations within the active area appearing shortly before thermal breakdown (see Appendix D.2) may indicate such a delamination of the top contact, resulting in an alternation of good and bad physical as well as electrical contact to the organic semiconductor. The textural modification of the top contact within the blue dashed circle further supports this impression and reveals also the local temperature maximum in the center, as expected by an equal power distribution. However, an influence of evaporation of C_{60} within the active area applying pressure to the electrode cannot be excluded. After strip off,

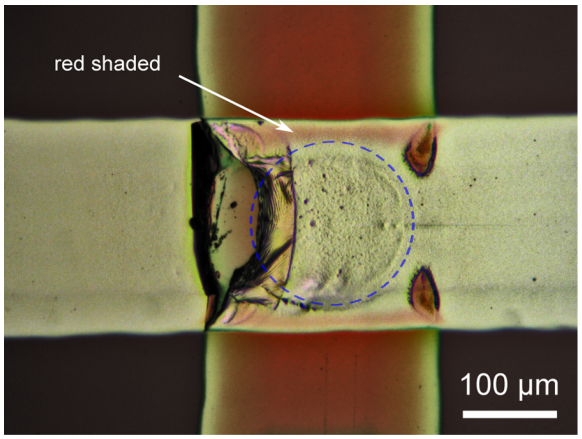

FIGURE 8. Picture of a device after breakdown. The top contact delaminates instead of shortcut to the bottom electrode. The strip off starts at the edges, where the heat is strongest. In the middle of the active area a blue dashed circle marks the area within the texture of the top Al electrode has significantly changed due to a local temperature maximum. Red shaded areas at top and bottom side of the active area suggest the hypothesis that C_{60} is deposited there caused by self-heating assisted evaporation of the molecules.

the metal film has neither connection to the organic thin film nor to the electrode, implicating a very high resistance.

8. CONCLUSION

For studying Joule self-heating in organic semiconductor devices, a detailed knowledge of the heat transport in the whole system is necessary. For that reason, stationary heat transport simulations are employed for visualizing the heat flow into the substrate glass. We are able to show that a typical quadratic organic thin film device behaves essentially like a circular disc heat source with negligible thickness if the substrate is at least three times thicker than the device width. In this limit, the result can be given by an analytical expression, revealing a thermal resistance in the range of 1000 K/W. Thermal imaging confirms this result and reveals a strong heating at the edges of the device. With homogenous distributed heat power this result can not be understood. But taking into account additional line heat sources, all qualitative aspects are reproduced, showing that the current transport differs strongly from a 1D-configuration. Especially if we consider a positive feedback between temperature and mobility, regions with current densities above the average will be affected first, leading to an amplification of imbalances. This suggests that even in the non self-heating regime, strong current contributions at the edges of the active area have to be expected. Our understanding of the heat transport will help us to investigate the effect of positive temperature feedback in organic semiconductors in more detail. However, for extraction of charge transport parameters, e.g. within the EGDM model, either multidimensional simulations have to be carried out, or true 1D structures have to be realized.

Acknowledgement

The authors thank IPMS Fraunhofer (Dresden) for use of the infrared camera. The work of Th. Koprucki has been supported by the Deutsche Forschungsgemeinschaft (DFG) within the collaborative research center SFB 787 Semiconductor Nanophotonics. The work leading to these results has received funding from the European Communitys Seventh Framework Programme under Grant Agreement No. FP7-267995 (NUDEV).

Appendix A. Supporting experimental figures

A.1. **Sample geometry.**

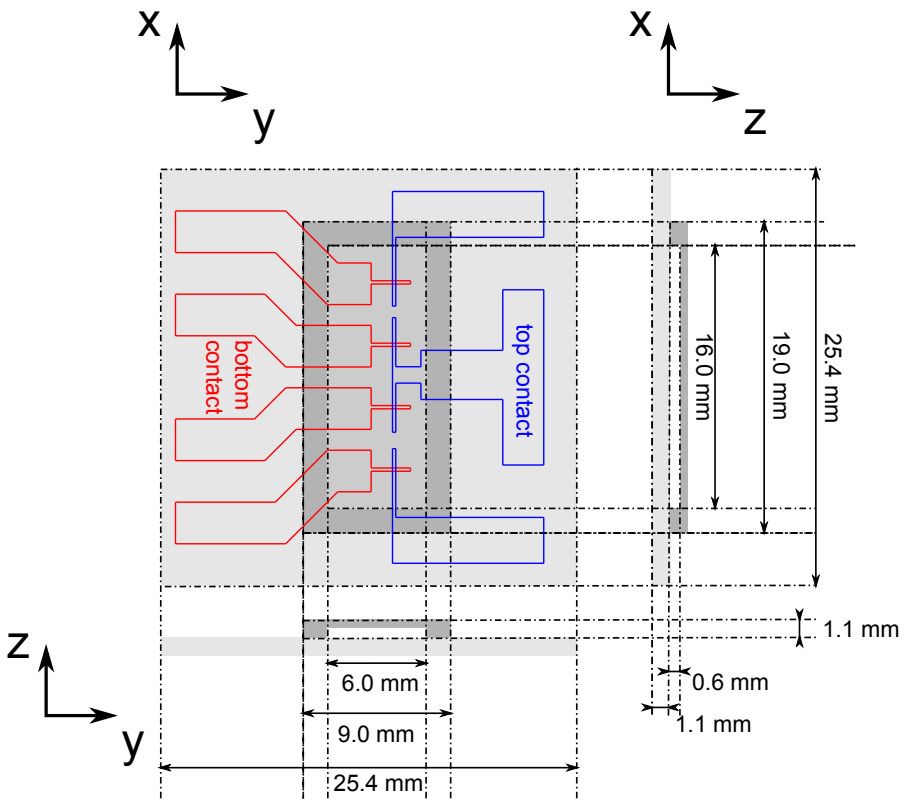

Figure A.1. Geometry of the substrate with four encapsulated samples in their respective dimensions.

Fig. A.1 shows a sketch of the quadratic substrate glass (width 25.4 mm) with mounted encapsulation glass, both with a thickness of 1.1 mm. An indentation (depth 0.6 mm) of the encapsulation orientated towards the active area prohibits a direct touch of the sensitive device structure. In there, the blue area defines the top contact whereas the red area forms the bottom contact. According to the design, the electrodes exhibit a width of 200 μm each in the active area.

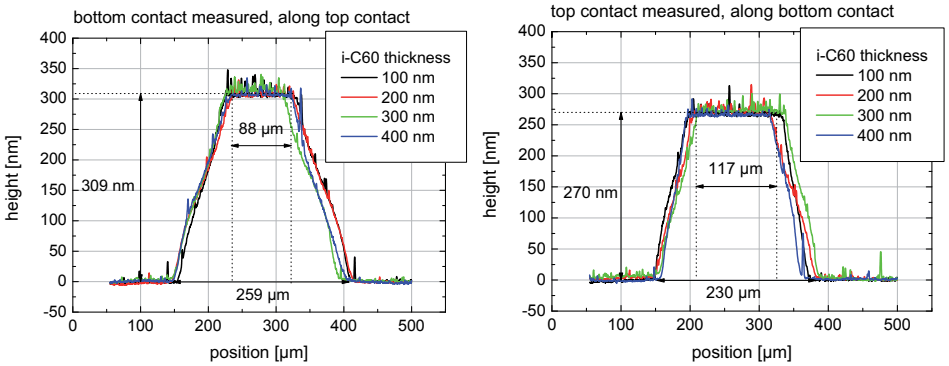

FIGURE A.2. Profilometer line scans of bottom (left) and top (right) contact.

The profiles of the electrodes are measured using a profilometer Veeco Dektak V9. The line scans are carried out along the top contact for analyzing the bottom contact and vice versa. The shape of the profiles is typically trapezoidal as a consequence of a certain distance between shadow masks and substrate during the evaporation process, see Fig. A.2. Moreover, the profile is independent on the i-C_{60} layer thickness. The contact angle of the profile is below 1° (note the length scales in the figure) and therefore the common organic layer thickness can be assumed to be constant between the electrodes. Furthermore both electrodes feature slanting sides with metal layer thicknesses below 10 nm over a range of around 500 nm. In this regions the electrode resistance can increase non-linearly with decreasing metal layer thickness due to a non-contiguous layer formation. Despite that the maximal thickness of the contacts is in good accordance to the evaporated metal layer thickness (300 nm).

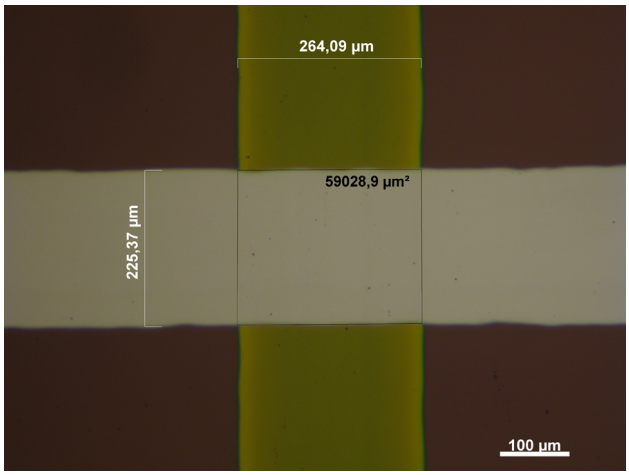

FIGURE A.3. Electrically active area formed by overlapping electrodes, image taken via optical microscope.

The structural broadening due to the evaporation process (see also Fig. A.2) directly affects the electrically active area of the samples. To be able to estimate a lower limit, we measure the electrodes including their overlap with a photocamera calibrated in terms of length and mounted on an optical microscope, see Fig. A.3. We obtain a mean of 0.06 mm^2 which agrees well with the preceding results and which is used later on to calculate current densities.

A.2. **Reversed bias.**

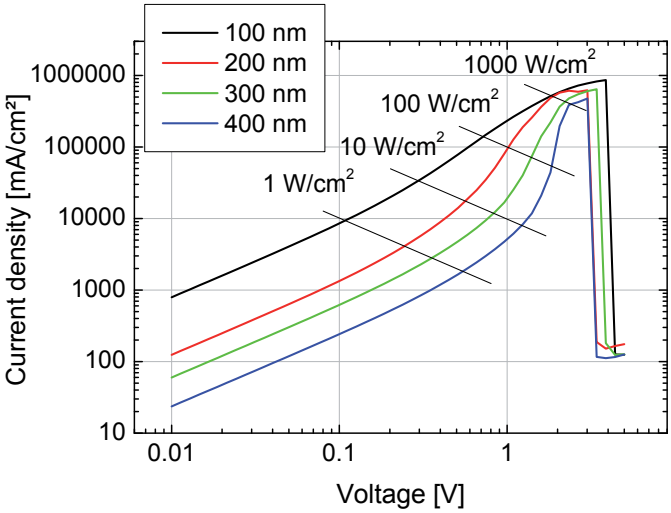

FIGURE A.4. IV characteristic of the test structure for reverse bias.

In Fig. A.4, we show the current-voltage characteristics for reverse bias in comparison to the measurements shown in the publication. Thus, the electron current flow is from bottom electrode to top electrode. Similar values for current and voltage are obtained, indicating no built-in potential and symmetric injection properties. Furthermore, a linear regime, a self-heating regime, and a breakdown regime as shown in the publication can be observed.

A.3. **Dependence of self-heating on measurement speed.**

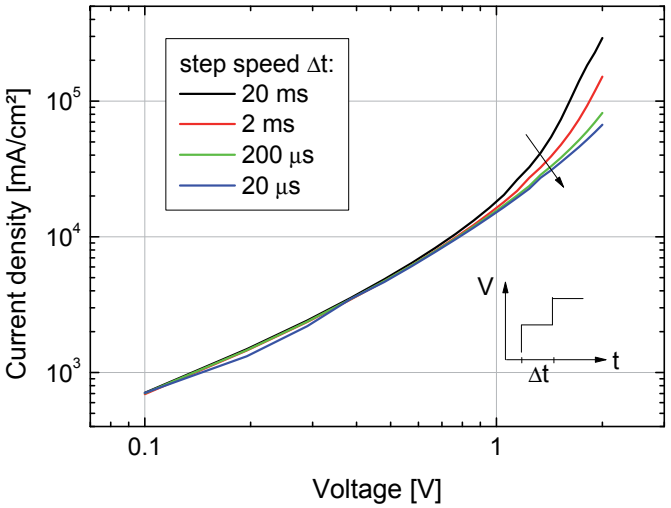

FIGURE A.5. The self-heating of a high mobility nin-device with 300 nm i-C_{60} can be reduced by applying faster measurement cycles.

Joule self-heating of the sample can be suppressed or even promoted by the choice of measurement speed while acquiring current-voltage characteristics. Above

the linear regime where a priori no self-heating occurs, the time per voltage step is crucial. In this self-heating regime the heat up of the device can be diminished if the voltage is applied only during a small time frame, cp. Fig. A.5. Consequently, the average electrical power is decreased, reducing the measureable power dissipation. Below 20 μs, up to a voltage of 2 V no self-heating is obtained anymore, see Fig. A.5. However, for the purpose of studying heat transport, if not stated differently a measurement interval of 20 ms is applied in our electrical characterization.

A.4. **Transient measurements.**

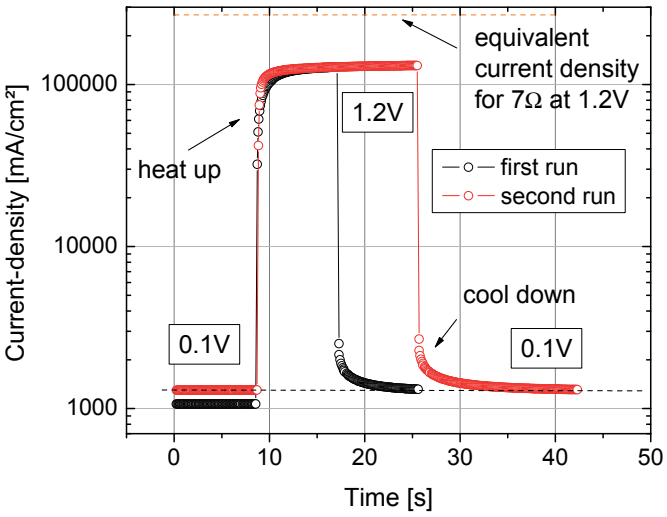

FIGURE A.6. Transient current characteristics in an nin test structure with 300 nm i-C_{60} .

The conducted current-transient measurements depict self-heating in our devices electrically. We perform voltage steps from 0.1 V up to 1.2 V and again down to 0.1 V at a rate of 100/200 (first/second run) measurement points per voltage and detect the current flow through the device. Once the voltage overcomes the linear regime where no change in current density is obtained (0.1 V), an increase of the current density by almost one order of magnitude clarifies the heat up of the device (1.2 V), see Fig. A.6. The upper dashed line in Fig. A.6 shows the maximum current density which is possible due to a series resistance of 7 Ω at a voltage of 1.2 V. The origin of the saturation of current density at 1.2 V could be this series resistance. When the voltage steps down to 0.1 V again, one observes the cool down process of the sample as temperature decreases and thereby the current density decays to equilibrium. In the first run, the current density reaches a slightly higher value compared to the start of the measurement. The strong self-heating could cause here some variation of the morphology of the layers forming the device. In the second run, no change is obtained, and the current density settles again at the initial value of 1300 mA/cm^2 at a voltage of 0.1 V (cf. Fig. A.6).

A.5. **Infrared camera measurements.**

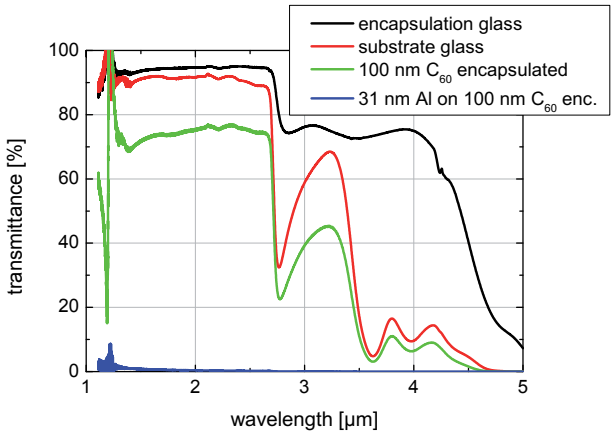

FIGURE A.7. Measured IR spectra in the wavelength range from 1 μm to 5 μm.

The temperature distribution of our electrically driven device is examined via an infrared thermo camera which is sensitive to wavelengths from 1.8 μm to 5 μm. In advance, it is important to be aware of the transmissive spectra of the materials employed. The glass substrate as well as the encapsulation glass show high transmittance up to 2.7 μm, see Fig. A.7. Thus, both permit a view onto the device. The encapsulation glass shows transmittance values over 70% even up to 4.0 μm. A C_{60}-layer of 100 nm thickness evaporated onto the glass substrate and covered by the encapsulation glass shows a transmittance which is strongly influenced by the substrate glass (cf. Fig. A.7).

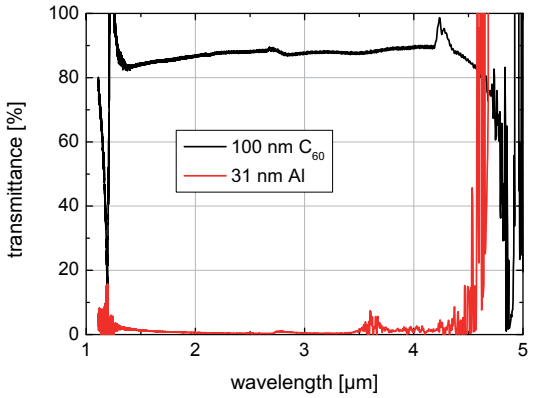

FIGURE A.8. Recalculated transmittance spectra for Al and C_{60} taking the spectra for substrate glass and encapsulation glass into account.

If we recalculate the transmittance spectrum of C_{60} by taking the spectra of the single substrate and encapsulation glass into account, the transmittance of 100 nm C_{60} is higher than 80% over nearly the whole measurement range as shown

in Fig. A.8. Above 4.5 μm the recalculated values are no more valid since the transmittance of the substrate and the encapsulation glass are very low. Thus, C_{60} is nearly transparent in the considered IR range and is not suited for calibration because background IR radiation would have to be taken into account. In contrast, the recalculated transmittance spectra of 100 nm Al reveals low values ($< 10\%$) in the relevant measurement range (cf. Fig. A.8). Again, above 4.5 μm the recalculated values for Al contain errors due to the low transmittance values of the substrate and the encapsulation glass. Nevertheless, Al it well suited for calibrating the temperature because no IR radiation from a source behind can be detected, so that only the radiative emission of Al itself contributes.

To calibrate the camera, we embed the sample into a massive copper block with a small slit above the encapsulation glass. Within the copper block two temperature sensors are included, one below and one above the sample. The temperature difference between the sensors is observed not to be higher than 0.1 K. Since the sample is located between the two temperature sensors, the temperature of the device must be in between and is thus well known. We calibrate the infrared camera after we set the sample to 343 K (70 °C) using a heat plate and achieve an agreement of applied temperature and temperature measured by IR emission. A calibration at higher temperatures is not possible because the permissible temperature of the infrared camera lens is 323 K (50°C) which is easily reached while monitoring the IR emission of a macroscopic target.

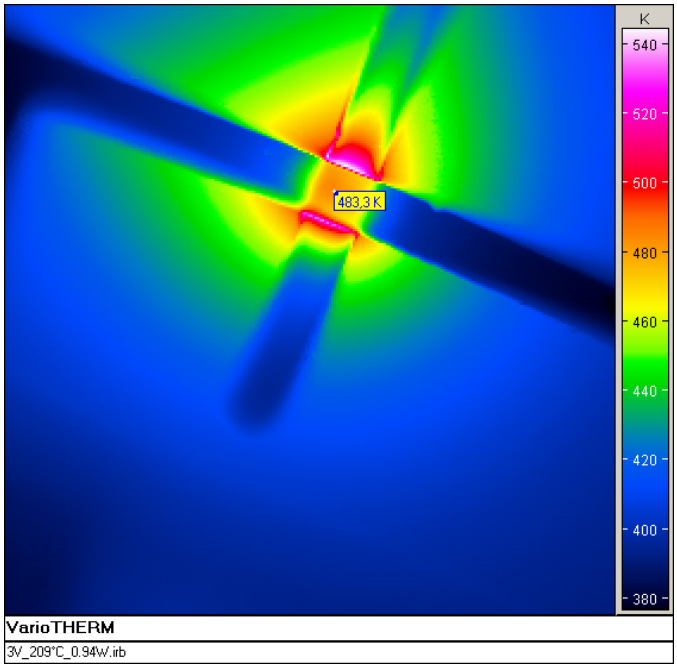

FIGURE A.9. A strong heat up in the center and at the edges of a 300 nm i-C_{60} sample is visible in infrared camera measurements, here shortly before breakdown.

The temperatures for the experimental estimation of thermal resistance are taken in the middle of the active area. Fig. A.9 is related to the last measurement point in Fig. 7 at a power of 0.94 W. At even higher voltages the device breaks down, as shown in `video2_thermal_breakdown.mp4` of the supporting information. The temperature distribution is not completely symmetric with respect to the electrodes.

The temperature is enhanced in the quarter between the electrodes where the potentials are applied, implying the influence of their series resistances on the power dissipation. All in all temperatures up to 483 K (210°C) are obtained in the middle of the active area. At the edges the temperature increases above 540 K (267°C).

A.6. **Temperature profiles.**

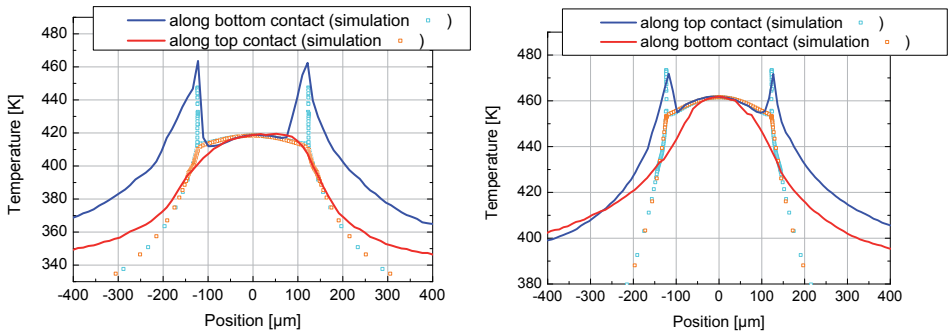

FIGURE A.10. Left: Measured temperature profiles of the sample in top view (lines). Right: Temperature profiles of the sample in bottom view. Results of the simulation are indicated by squares for the different line scan directions, respectively.

The temperature profiles of the experimental data (Fig. A.10, (closed lines)) are taken along the middle of the electrodes, similar to the height profiles. For top view (cf. Fig. 6) we clearly see the two peaks of the heated edges if we scan along the bottom contact. Nevertheless, a local maximum is present in the sample center between the temperature peaks (global maximum). If we scan along the top contact, only a global maximum is visible, in agreement with the local maximum of the scan along the bottom contact. No influence of the heated edges onto the temperature distribution can be obtained for this measurement direction. For the bottom view (Fig. A.10) we have found similar results. However the peaks are not that strongly pronounced. This behavior is consistent with the simulation results (Fig. A.10, (squares)). It can be explained by the higher thermal resistance for heat dissipation at line sources near the top contact in comparison to heat dissipation at line sources close to the substrate glass. Additionally, the heated glass substrate will blur out the temperature distribution measured by IR emission.

For comparison with the line scans of the simulation we have adjusted the distance between the experimental obtained temperature peaks to 245 μm and the power used in the simulation is chosen to get equal temperatures at the center position. Therefore, we used a power of 0.115 W for the top view and 0.155 W for the bottom view. This is in accordance to the estimation of the thermal resistance where also the center of the active area is used for comparison and thus, we achieve similar temperature ranges between experimental and simulated results for top and bottom view. Please note that due to the linearity of the solution of the heat transport equation the shape of the temperature profile is independent of the dissipated power.

Again, the temperature peaks are more pronounced for the top view (through the encapsulation glass) than for the bottom view (through the substrate glass) and are in general broadened for the experimental data, see Fig. A.10. The different shape of the measured and simulated peaks shows, that the line heat sources are in reality rather a certain power distribution which is very sharp near the active area and decreases more slowly with increasing distance to the active area. Since the

real spatial profile of the dissipative power near the contact edges is unknown, the assumption of line heat sources describing the dissipative power at the edges in a lumped way is a suitable way to reach a qualitative understanding.

At distances more than 200 μm from the center position, the decrease of the temperature is slower than predicted by the simulation. As shown in the video `video3_sample.mp4` of the supporting information the substrate heats up due to continuos power supply leading to a temperature rise in the environment of the substrate.

A.7. **Thermal breakdown.**

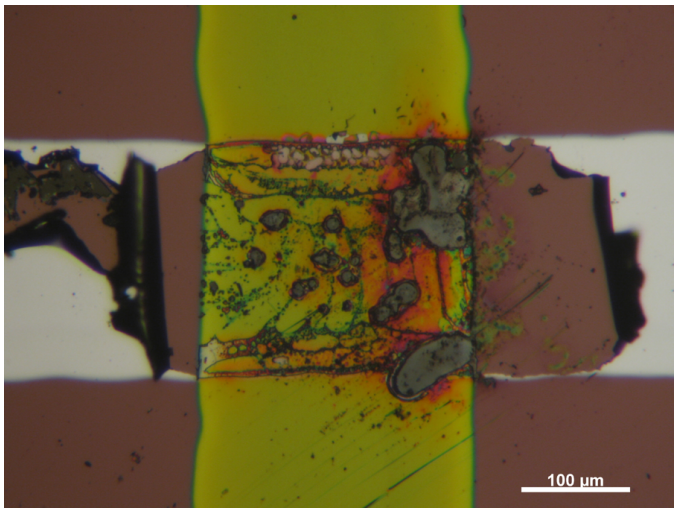

FIGURE A.11. Major damage to the whole top contact after applying instantly 5 V to the device.

As shown in the publication, the contact breaks preferably at the edge of the top contact which is closer to the connection of the applied voltage if we increase the the voltage from 0.01 V to 5 V in logarithmic steps. If a potential of 5 V is applied instantly the top contact immediately tears. The whole top contact is delaminated and coiled (cf. Fig. A.11).

Appendix B. Supporting simulation figures

B.1. **Heat flow simulation resulting in a homogeneous temperature distribution in the active area.**

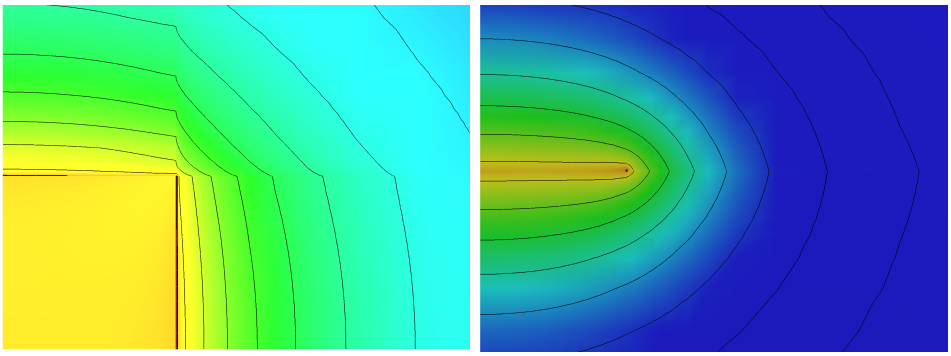

Figure B.1. Cross-sections of computed 3D temperature distributions for dissipative power 0.1 W. The heat sources describing the dissipative power is a mixture of an equally distributed power dissipation and line heat sources, cp. Figure 4 in Sec. 5, too. The proportion assigned to the edges is chosen as $\beta = 0.67$ resulting in a homogeneous temperature distribution within the active area. Left: Lateral cross-section. Right: Vertical cross-section.

B.2. **Thermal resistance by 3D simulation and analytical approximation.**

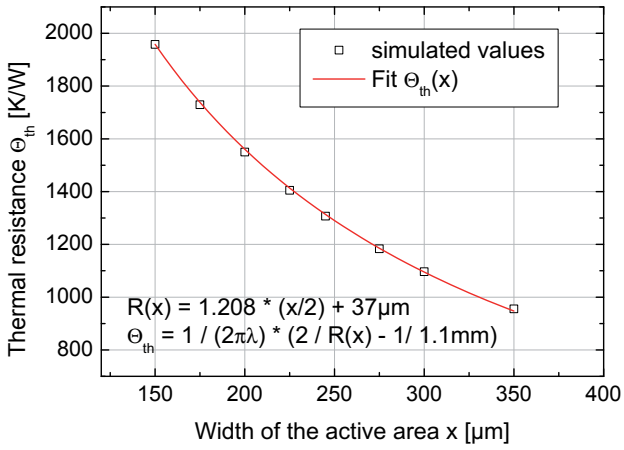

Figure B.2. Thermal resistance from 3D numerical simulations (squares) compared to analytical approximations (solid line) for the case of a homogeneous heat source.

In the comparison between the thermal resistance obtained from 3D numerical simulations of the squared active area (with width L_0 and a homogeneous heat source) to the analytical solution for constant heat supply over a circular area (with radius R) given by

$$\Theta_{\mathrm{th}}(L_0) = \frac{1}{2\pi\lambda}\left(\frac{2}{R} - \frac{1}{H_{\mathrm{sub}}}\right)$$

we used for the effective radius

$$R = 1.208\frac{L_0}{2} + 37\,\mu\text{m}$$

and a substrate thickness of $H_{\text{sub}} = 1.1\,\text{mm}$ (cf. Fig. B.2). Please note that this fit is only possible for device geometries with sufficiently large substrate thicknesses, $H_{\text{sub}} > 3R$.

Appendix C. Heat conduction in infinite half space due to heat supply over a circular disc

We use the notation of Sec. 5. Especially let λ be the heat conductivity and R the radius of the disc, see inset of Fig. 5.

C.1. **Homogeneous heat flux q through circular disc $\Gamma_\mathbf{d}$.** According to [29, p. 216] the analytical solution of the heat flow equation in the infinite half space is given by

$$T(r_\parallel, z) = \frac{qR}{\lambda}\int_0^\infty e^{-tz} J_0(tr_\parallel) J_1(tR)\frac{dt}{t},$$

where J_0 and J_1 denote Bessel functions of the first kind. The total heat flow $\dot{Q}$ through the circular area Γ_d results in

$$\dot{Q} = q\pi R^2.$$

Using $J_0(0) = 1$ and (Watson 44, p. 45 and p. 386)[2] the temperature distribution on symmetry axis ($r_\parallel = 0$) $T_2(z) = T(r_\parallel = 0, z)$ is calculated by

$$\begin{aligned} T_2(z) =& \frac{qR}{\lambda}\int_0^\infty e^{-tz} J_1(tR)\frac{dt}{t} \\ =& \frac{qR}{2\lambda}\int_0^\infty e^{-tz}\Big(J_0(tR) + J_2(tR)\Big)dt \\ =& \frac{qR^2}{2\lambda}\left[\frac{1}{\sqrt{z^2+R^2}} + \frac{\left(\sqrt{z^2+R^2} - z\right)^2}{R^2\sqrt{z^2+R^2}}\right] \\ =& \frac{q}{\lambda}\Big(\sqrt{z^2+R^2} - z\Big). \end{aligned} \tag{17}$$

From Eq. (17) we derive the far-field behavior $z \to \infty$ on the symmetry axis by a series expansion in terms of $\frac{R}{z}$:

$$T_{2,\text{far}}(z) = \frac{qR}{2\lambda}\Big(\frac{R}{z} - \frac{1}{4}\Big(\frac{R}{z}\Big)^3\Big) + \mathcal{O}\left(\Big(\frac{R}{z}\Big)^5\right) = \frac{\dot{Q}}{2\pi\lambda}\frac{1}{z} + \mathcal{O}\left(\Big(\frac{R}{z}\Big)^3\right).$$

The maximum temperature on the disc Γ_d is given by

$$T_{\text{d,max}} = T_2(z=0) = \frac{q}{\lambda}R = \frac{\dot{Q}}{\pi\lambda R}.$$

The minimum temperature on the disc Γ_d is attained at the boundary $r_\parallel = R$ and can be calculated using (Watson 44, p. 44 and p. 386)[2]

$$\begin{aligned} T_{\text{d,min}} = T(r_\parallel = R, 0) &= \frac{qR}{\lambda}\int_0^\infty J_0(tR)J_1(tR)\frac{dt}{t} = \frac{qR}{\lambda}\,\frac{2}{\pi}\sin\frac{\pi}{2} \\ &= \frac{2}{\pi}T_{\text{d,max}}. \end{aligned}$$

[2] G. N. Watson. *A treatise on the theory of Bessel functions.* Cambridge Mathematical Library. Cambridge University Press, Cambridge, 1995. Reprint of the second (1944) edition.

C.2. **Homogeneous temperature on circular disc Γ_d.** In this case we obtain the temperature distribution

$$T(r_\parallel, z) = \frac{2T_d}{\pi} \arcsin\left\{ \frac{2R}{\left[(r_\parallel - R)^2 + z^2\right]^{1/2} + \left[(r_\parallel + R)^2 + z^2\right]^{1/2}} \right\}$$

and the total heat flow $\dot{Q}$ through the circular disc Γ_d results in

$$\dot{Q} = 4\lambda T_d R = -2\pi\lambda \int_0^R \left(\frac{\partial T}{\partial z}\right)\Big|_{z=0} r\, dr,$$

see [29, p. 215]. We consider the temperature profile on the symmetry axis $T_3(z) = T(r_\parallel = 0, z)$ and discuss its far-field behavior $z \to \infty$ by a series expansion in terms of $\frac{R}{z}$:

$$T_{3,\mathrm{far}}(z) = \frac{2T_d}{\pi}\left(\frac{R}{z} - \frac{1}{3}\left(\frac{R}{z}\right)^3\right) + \mathcal{O}\left(\left(\frac{R}{z}\right)^5\right) = \frac{\dot{Q}}{2\pi\lambda}\frac{1}{z} + \mathcal{O}\left(\left(\frac{R}{z}\right)^3\right).$$

Appendix D. Supporting videos of IR camera measurements

D.1. **Transient of voltage step:** `video1_transient.mp4`**.** The video is taken while thermal imaging. The result is similar to the electrical transient measurements presented already in Fig. A.6. Likewise, a voltage step is applied, from 0.1 V up to here 2.0 V and down back to 0.1 V. While at the lower voltage, no temperature increase is obtained, one detects strong self-heating and a strongly increased temperature of the device after driving it at the higher voltage for 1 s. By reducing the applied voltage to 0.1 V again, the device after cools down. At this stage, the falling temperature can be measured electrically.

D.2. **Thermal breakdown:** `video2_thermal_breakdown.mp4`**.** The video shows the thermal breakdown of the device at a voltage of 3.6 V. We apply a voltage of 3.3 V and increase the voltage up to 3.6 V in consecutive steps of 0.1 V. Please note that the temperature scale bar does automatically rescale to show all the time the full temperature resolution. Shortly before the top contact begins to tear, the temperature distribution within the active area starts to oscillate , indicating a possible delamination process. This behavior is also shown by the top contact ripped halfway through which seems to swing before it finally tears.

D.3. **Heating of whole sample:** `video3_sample.mp4`**.** The video shows the heat up of the whole sample at an applied voltage of 1.4 V. Since the process proceeds quite slowly we use a quintuple time lapse. At the end of the video the mask layout shown in Fig. A.1 can be recognized. At the top side the encapsulation glass is supporting the heat transport leading to a broadening of the temperature distribution. This measurement shows that without cooling the substrate, after a certain duration even neighboring devices could be influenced.

References

[1] H. Kleemann, A. Zakhidov, M. Anderson, T. Menke, K. Leo, B. Lüssem, Direct structuring of C_{60} thin film transistors by photo-lithography under ambient conditions, Organic Electronics 13 (3) (2012) 506–513.

[2] M. A. McCarthy, B. Liu, E. P. Donoghue, I. Kravchenko, D. Y. Kim, F. So, A. G. Rinzler, Low-voltage, low-power, organic light-emitting transistors for active matrix displays, Science 332 (6029) (2011) 570–573.

[3] A. J. Ben-Sasson, E. Avnon, E. Ploshnik, O. Globerman, R. Shenhar, G. L. Frey, N. Tessler, Patterned electrode vertical field effect transistor fabricated using block copolymer nanotemplates, Appl. Phys. Lett. 95 (21) (2009) 213301.

[4] K. Nakayama, S. Fujimoto, M. Yokoyama, Improvement in the on/off ratio of a vertical-type metal-base organic transistor by heat treatment in air, Org. Electron. 10 (3) (2009) 543–546.
[5] W. F. Pasveer, J. Cottaar, C. Tanase, R. Coehoorn, P. A. Bobbert, P. W. M. Blom, D. M. de Leeuw, M. A. J. Michels, Unified description of charge-carrier mobilities in disordered semiconducting polymers, Phys. Rev. Lett. 94 (20) (2005) 206601.
[6] M. Slawinski, D. Bertram, M. Heuken, H. Kalisch, A. Vescan, Electrothermal characterization of large-area organic light-emitting diodes employing finite-element simulation, Org. Electron. 12 (8) (2011) 1399–1405.
[7] T. Matsushima, H. Sasabe, C. Adachi, Carrier injection and transport characteristics of copper phthalocyanine thin films under low to extremely high current densities, Appl. Phys. Lett. 88 (3) (2006) 033508–3.
[8] T. Matsushima, C. Adachi, Observation of extremely high current densities on order of MA/cm^2 in copper phthalocyanine thin-film devices with submicron active areas, Jpn. J. Appl. Phys. 46 (47) (2007) L1179–L1181.
[9] S. Steudel, K. Myny, V. Arkhipov, C. Deibel, S. De Vusser, J. Genoe, P. Heremans, 50 MHz rectifier based on an organic diode, Nat. Mater. 4 (8) (2005) 597–600.
[10] S. Sze, K. K. NG, Physics of Semiconductor Devices, 3rd Edition, John Wiley and Sons, 2007.
[11] N. Karl, Charge carrier transport in organic semiconductors, Synthetic Metals 133-134 (2003) 649–657.
[12] K. Hannewald, P. A. Bobbert, Anisotropy effects in phonon-assisted charge-carrier transport in organic molecular crystals, Phys. Rev. B 69 (7) (2004) 075212.
[13] A. Miller, E. Abrahams, Impurity conduction at low concentrations, Phys. Rev. 120 (3) (1960) 745–755.
[14] H. Bässler, Charge transport in disordered organic photoconductors a monte carlo simulation study, phys. stat. sol. (b) 175 (1) (1993) 15–56.
[15] R. Coehoorn, W. F. Pasveer, P. A. Bobbert, M. A. J. Michels, Charge-carrier concentration dependence of the hopping mobility in organic materials with gaussian disorder, Phys. Rev. B 72 (15) (2005) 155206.
[16] K. Walzer, B. Maennig, M. Pfeiffer, K. Leo, Highly efficient organic devices based on electrically doped transport layers, Chem. Rev. 107 (4) (2007) 1233–1271.
[17] M. Schober, M. Anderson, M. Thomschke, J. Widmer, M. Furno, R. Scholz, B. Lüssem, K. Leo, Quantitative description of charge-carrier transport in a white organic light-emitting diode, Phys. Rev. B 84 (16) (2011) 165326.
[18] D. Im, H. Moon, M. Shin, J. Kim, S. Yoo, Towards gigahertz operation: Ultrafast low turn-on organic diodes and rectifiers based on C_{60} and tungsten oxide, Adv. Mater. 23 (5) (2011) 644–648.
[19] A. Fischer, P. Siebeneicher, H. Kleemann, K. Leo, B. Lüssem, Bidirectional operation of vertical organic triodes, J. Appl. Phys. 111 (4) (2012) 044507–8.
[20] S. Kobayashi, T. Takenobu, S. Mori, A. Fujiwara, Y. Iwasa, C_{60} thin-film transistors with high field-effect mobility, fabricated by molecular beam deposition, Sci. Tech. Adv. Mater. 4 (4) (2003) 371–375.
[21] F. Cotton, P. Huang, C. A. Murillo, D. J. Timmons, A complete series of $W_2(hpp)_4Cl_n$ (n=0,1,2) compounds, Inorganic Chemistry Communications 5 (7) (2002) 501–504.
[22] T. Menke, D. Ray, J. Meiss, K. Leo, M. Riede, In-situ conductivity and seebeck measurements of highly eficient n-dopants in fullerene C_{60}, Appl. Phys. Lett. (2012) doi:10.1063/1.3689778.
[23] Z. Racz, J. He, S. Srinivasan, W. Zhao, A. Seabaugh, K. Han, P. Ruchhoeft, J. Wolfe, Nanofabrication using nanotranslated stencil masks and lift off, J. Vac. Sci. Technol. B 22 (1) (2004) 74–76.
[24] T. Matsushima, C. Adachi, High-current injection and transport on order of kA/cm^2 in organic light-emitting diodes having mixed organic/organic heterojunction interfaces, Jpn. J. Appl. Phys. 46 (35) (2007) L861–L863.
[25] J. Fuhrmann, T. Streckenbach, H. Langmach, M. Uhle, pdelib2: Software components for pdes., URL (2012-02-27): http://pdelib.org (2012).
[26] H. Si, K. Gärtner, J. Fuhrmann, Boundary conforming Delaunay mesh generation, Comput. Math. Math. Phys. 50 (2010) 38–53.
[27] O. Schenk, K. Gärtner, G. Karypis, S. Röllin, M. Hagemann, PARDISO Solver Project, URL: http://www.pardiso-project.org, retrieved 2012-02-05 (2012).
[28] K. Gärtner, O. Schenk, Solving unsymmetric sparse systems of linear equations with PARDISO, Journal of Future Generation Computer Systems 20 (3) (2004) 475–487.
[29] H. S. Carslaw, J. C. Jaeger, Conduction of heat in solids, 2nd Edition, Oxford Science Publications, The Clarendon Press Oxford University Press, New York, 1959.

[30] F. Li, A. Werner, M. Pfeiffer, K. Leo, X. Liu, Leuco crystal violet as a dopant for n-doping of organic thin films of fullerene C_{60}, J. Phys. Chem. B 108 (44) (2004) 17076–17082.
[31] W. Krätschmer, L. D. Lamb, K. Fostiropoulos, D. R. Huffman, Solid C_{60}: a new form of carbon, Nature 347 (6291) (1990) 354–358.